Computer Methods in Biomechanics and Biomedical Engineering

Publication details, including instructions for authors and subscription information:
http://www.tandfonline.com/loi/gcmb20

Haemodynamic impact of stent-vessel (mal)apposition following carotid artery stenting: mind the gaps!

G. De Santis [a], M. Conti [b], B. Trachet [a], T. De Schryver [a], M. De Beule [a], J. Degroote [c], J. Vierendeels [c], F. Auricchio [b], P. Segers [a], P. Verdonck [a] & B. Verhegghe [a]

[a] BiTech-bioMMeda, Ghent University, Ghent, Belgium

[b] Department of Structure Mechanics, University of Pavia, Pavia, Italy

[c] Department of Flow, Heat and Combustion Mechanics, Ghent University, Ghent, Belgium

Version of record first published: 08 Dec 2011.

To cite this article: G. De Santis , M. Conti , B. Trachet , T. De Schryver , M. De Beule , J. Degroote , J. Vierendeels , F. Auricchio , P. Segers , P. Verdonck & B. Verhegghe (2011): Haemodynamic impact of stent-vessel (mal)apposition following carotid artery stenting: mind the gaps!, Computer Methods in Biomechanics and Biomedical Engineering, DOI:10.1080/10255842.2011.629997

To link to this article: http://dx.doi.org/10.1080/10255842.2011.629997

Computer Methods in Biomechanics and Biomedical Engineering
iFirst article, 2011, 1–12

Haemodynamic impact of stent–vessel (mal)apposition following carotid artery stenting: mind the gaps!

G. De Santis[a]*, M. Conti[b], B. Trachet[a], T. De Schryver[a], M. De Beule[a], J. Degroote[c], J. Vierendeels[c], F. Auricchio[b], P. Segers[a], P. Verdonck[a] and B. Verhegghe[a]

[a]*BiTech-bioMMeda, Ghent University, Ghent, Belgium;* [b]*Department of Structure Mechanics, University of Pavia, Pavia, Italy;* [c]*Department of Flow, Heat and Combustion Mechanics, Ghent University, Ghent, Belgium*

(*Received 20 June 2011; final version received 4 October 2011*)

Carotid artery stenting (CAS) has emerged as a minimally invasive alternative to endarterectomy but its use in clinical treatment is limited due to the post-stenting complications. Haemodynamic actors, related to blood flow in the stented vessel, have been suggested to play a role in the endothelium response to stenting, including adverse reactions such as in-stent restenosis and late thrombosis. Accessing the flow-related shear forces acting on the endothelium *in vivo* requires space and time resolutions which are currently not achievable with non-invasive clinical imaging techniques but can be obtained from image-based computational analysis. In this study, we present a framework for accurate determination of the wall shear stress (WSS) in a mildly stenosed carotid artery after the implantation of a stent, resembling the commercially available Acculink (Abbott Laboratories, Abbott Park, Illinois, USA). Starting from angiographic CT images of the vessel lumen and a micro-CT scan of the stent, a finite element analysis is carried out in order to deploy the stent in the vessel, reproducing CAS *in silico*. Then, based on the post-stenting anatomy, the vessel is perfused using a set of boundary conditions: total pressure is applied at the inlet, and impedances that are assumed to be insensitive to the presence of the stent are imposed at the outlets. Evaluation of the CAS outcome from a geometrical and haemodynamic perspective shows the presence of atheroprone regions (low time-average WSS, high relative residence time) colocalised with stent malapposition and stent strut interconnections. Stent struts remain unapposed in the ostium of the external carotid artery disturbing the flow and generating abnormal shear forces, which could trigger thromboembolic events.

Keywords: carotid artery stenting; computational fluid dynamics; pyFormex; finite element analysis; image-based analysis; impedance model

1. Introduction

Focal manifestations of atherosclerotic diseases, such as stenoses and aneurysms, are often treated with stenting as a minimally invasive procedure aiming to modify the arterial flow locally. In case of a stenosed carotid artery, a stent is implanted to reopen the vessel by pushing the stenosis away from the lumen, thus reducing the hydraulic resistance at the diseased location and restoring the cerebral flow to a physiological level. The limited long-term success of carotid artery stenting (CAS), reported from large population clinical studies (Brott et al. 2010; Ederle et al. 2010; Paraskevas et al. 2010; Bangalore et al. 2011), has stimulated extensive research to (i) disclose the physical link between an adverse post-interventional biological response and the mechanical impact of stents and to (ii) explore better design/material possibilities. Stent thrombosis may develop on the basis of in-stent restenosis which is a consequence of prolonged inflammatory processes in the stented-vessel wall with excessive myointimal proliferation (Shah 2003; Li and Kleinstreuer 2005). In-stent restenosis is considered the main reason for CAS failure and has been associated, among others, with blood flow disturbances established after stenting (Groschel et al. 2005; Ener et al. 2008; Cosottini et al. 2010).

Most research focused on the performance of stents *per se* (e.g. radial stiffness and flexibility) (Carnelli et al. 2011), the stent–vessel interaction from a structural perspective (e.g. vessel stress and lumen gain) (Auricchio et al. 2011) or the effect of the stent on the vessel flow from a fluid dynamic perspective (Pant et al. 2010). However, investigating the stented-vessel haemodynamics ideally first requires a structural analysis, to obtain the post-implantation domain, followed by a fluid dynamic analysis (Balossino et al. 2008) or fluid–structure interaction analysis (Li and Kleinstreuer 2005). Recently, a geometrical algorithm to reproduce the post-stenting configuration has been proposed (Appanaboyina et al. 2008). However, such an approach neglects the structural impact of the stent in the diseased vessel, which introduces large deformations in the vessels and imperfect stent-to-vessel apposition, due to the compliance mismatch between the stiffer metal stent structure and the softer arterial tissue.

*Corresponding author. Email: gianluca.desantis@ugent.be

ISSN 1025-5842 print/ISSN 1476-8259 online

http://dx.doi.org/10.1080/10255842.2011.629997
http://www.tandfonline.com

In this paper, we provide a full-scale approach integrating the finite element method (FEM) and computational fluid dynamics (CFD) to predict the impact of stenting on patient-specific haemodynamics established after CAS. As a first step, a stent is virtually implanted in a mildly stenosed carotid artery using the FEM; then, the stented lumen is virtually perfused, reproducing realistic blood flow conditions using CFD. A critical step in this work is the development of a strategy to convert an FE model of a stented artery into a CFD model with the minimal loss of geometrical detail.

2. Methods

Modelling stented-vessel haemodynamics starting from medical images of the unstented configuration requires four serial steps: image-based stent deployment, computational model conversion, vessel perfusion and separated post-processing, as described below.

2.1 *Image-based stent deployment using the FEM*

A stent model, reconstructed from a micro-CT scan of the commercially available Acculink stent (Abbott), was virtually implanted in an image-based stenosed carotid artery using the FEM, as previously described in Auricchio et al. (2011) and validated against experimental data in Conti et al. (2011). Briefly, DICOM CTA images of a stenosed carotid artery of an 85-year-old male (24% in area reduction with respect to the non-stenosed vessel) were segmented to generate the arterial lumen surface. The arterial wall was not visible from the angiographic images and was reconstructed by assigning a wall thickness equal to 30% of the local radius in the healthy regions, and by proximal to distal surface interpolation in the stenotic regions (thicker wall), as reported in a previous study (De Santis et al. 2011). The self-expanding Nitinol stent (a self-expanding stent, different from balloon-expanding stent, deploys as a spring when released from a sheath, without need for balloon-induced plastic deformation) was inserted in a cylindrical tube (i.e. the sheath). After structured hexahedral meshing of vessel and stent, the sheath was shrinked, bent and positioned inside the stenosed vessel using the FEM (Abaqus/Explicit, Providence, RI, USA), thus prestressing the stent (inside the sheath) into a crimped and curved configuration. The sheath was then gradually released in a quasi-static process, enabling stent expansion against the vessel wall, until the equilibrium configuration was reached (i.e. the post-stenting vessel–stent configuration, Figure 1). The vessel tissue was modelled using the isotropic hyperelastic material proposed by Prendergast et al. (2003), without differentiating the stenotic region from the rest of the vessel. Boundary conditions (BCs) were defined at the boundaries in order to allow only radial displacement at the ending sections. The superelastic behaviour of Nitinol was modelled using a previously described material model, implemented in Abaqus with a user material subroutine (Auricchio et al. 1997). These assumptions were considered acceptable as the scope of the analysis was to obtain a realistic post-stenting shape of vessel and stent.

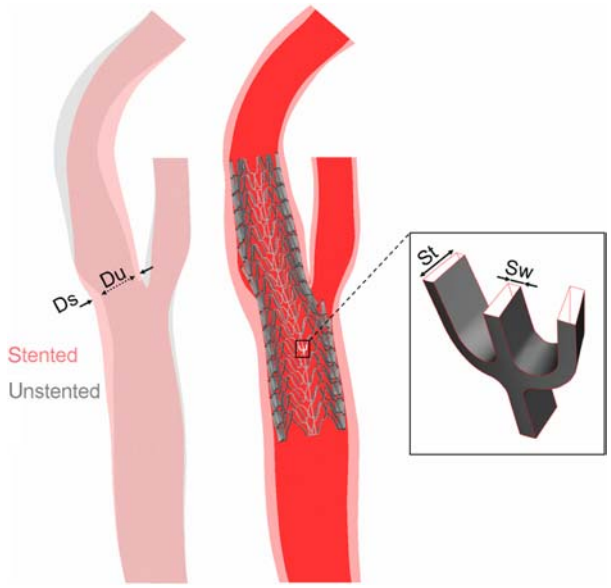

Figure 1. Carotid artery stenting using image-based FE analysis. Left: transparent view of the unstented and stented lumen (shown without stent struts). The indicated chord measured 4.2 mm before stenting (Du) and 5.6 mm after stenting (Ds). Centre: open view of arterial wall (pink), lumen surface (red) and stent struts (grey). Right: a detail of the stent is enlarged. Dimension used for strut thickness (St) and strut width (Sw) are 240 and 100 μm, respectively.

2.2 *Converting the FEM model into a CFD model*

Both deformed vessel and stent meshes were separately exported into pyFormex [an open-source software for generating, manipulating and transforming large geometrical models of 3D structures by sequences of mathematical transformations, currently under development at Ghent University (http://www.pyformex.org)], to be converted into a model suitable for CFD simulation of blood flow. The inner vessel surface, extracted from the arterial wall using a feature angle separation (if the angle between two adjacent faces' normals is higher than the chosen feature angle, the common adjacent edge identifies a geometrical edge; closed loops of geometrical edges can be used to partition a surface), and the stent surface represented two boundaries for the blood flow.

The flow domain in the stented artery was extracted by a Boolean subtraction of the stent volume from the

post-stenting lumen volume. In practice, this operation produces a surface that does not bind a meshable volume, with non-manifold edges, self-intersecting triangles and finite gaps. Such spurious features are the results of (i) numerical approximations occurring in the Boolean operation when the stent surface is close to or in contact with the vessel surface and (ii) the contact algorithm used in the FE solver, which generates a contact pressure when the contacting surfaces are at a non-zero distance. Such problems are common when performing Boolean operations on real shapes and can be solved by setting a tolerance during the Boolean operation or by cleaning the final surface using a smoothing algorithm (combined with manual intervention). Both approaches are not advisable when dealing with stents because they require a geometrical tolerance comparable to the stent strut size, with risk of losing the cross-sectional strut shape or even filtering out the strut. Therefore, an *ad hoc* approach, based on surface triggering, has been developed to prepare the stent surface before the Boolean subtraction. The distance between the outer stent surface and the inner vessel surface was computed using the VMTK script *vmtksurfacedistance* [http://www.vmtk.org] to assign the distance from the vessel endothelium to each stent node. The stent was considered to be locally in contact with the vessel (well apposed) or locally detached from the vessel (unopposed) if the nodal distance was smaller or higher than a threshold, respectively. The triangles containing well-apposed nodes were extruded slightly outside the lumen surface, in order to remove any negligible gap (i.e. a gap smaller than the threshold). With this operation, carried out using pyFormex, the stent surface was triggered with respect to the inner vessel surface, appearing either inside or outside the lumen (modelling a gap or a contact, respectively), but never in the region within the threshold distance from the vessel surface. By subtracting the volume defined by the triggered stent surface from the volume defined by the lumen surface [using the Boolean operation implemented in the GTS library embedded in pyFormex (http://gts.sourceforge.net/)], a new closed surface was generated, defining the boundary of the flow domain in the lumen of the stented artery (i.e. the volume difference). This surface still contained a number of spurious features (about 50), such as non-manifold edges (i.e. edges connecting more than two triangles) and intersecting triangles that could be easily detected, using the GTS library, and fixed, using Mimics (http://www.materialise.com/mimics). As a comparison, the surface generated without triggering the stent surface included about 2000 defects, making the manual reparation practically impossible (Figure 2).

Cylindrical flow extensions with a length of six times the local radius were added at the inlet and outlets in the directions of the centrelines using VMTK to facilitate the application of BCs. Longer extensions could not be applied because the flow extension of the external carotid artery (ECA) would have intersected the internal carotid artery (ICA), compromising the CFD computation (Figure 3(a)). The surface model, representing only the wet portion of the vessel wall and the stent together with the flow extensions, was used to generate an unstructured tetrahedral mesh (Figure 3(a)). Despite the proven advantages of structured hexahedral meshes over tetrahedral meshes for the arterial CFD analysis (De Santis et al. 2010), hexahedral meshing

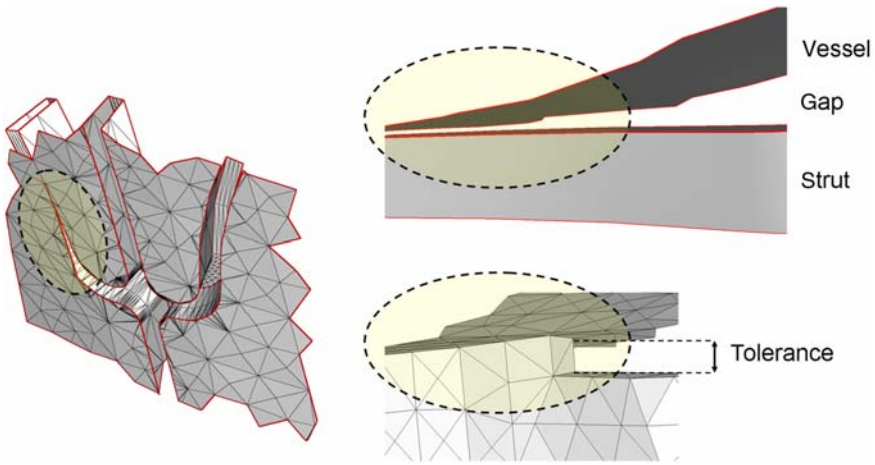

Figure 2. Stent-surface triggering onto the vessel surface. Left: if the Boolean subtraction is applied to the non-triggered stent, a smooth transition between the contacting (well apposed) and non-contacting (malapposed) regions appears, producing a very thin volume between the stent and the vessel, which cannot be filled with a computational mesh (the region of the stent detail is also shown in Figure 1). Right: with the triggering operation, a strut approaching the vessel surface (top) is deformed when the distance from the vessel surface is below a threshold. As a result, the Boolean subtraction produces a sharp transition, which avoids the generation of very thin volumes (bottom). The transition from contact to non-contact is highlighted in all cases.

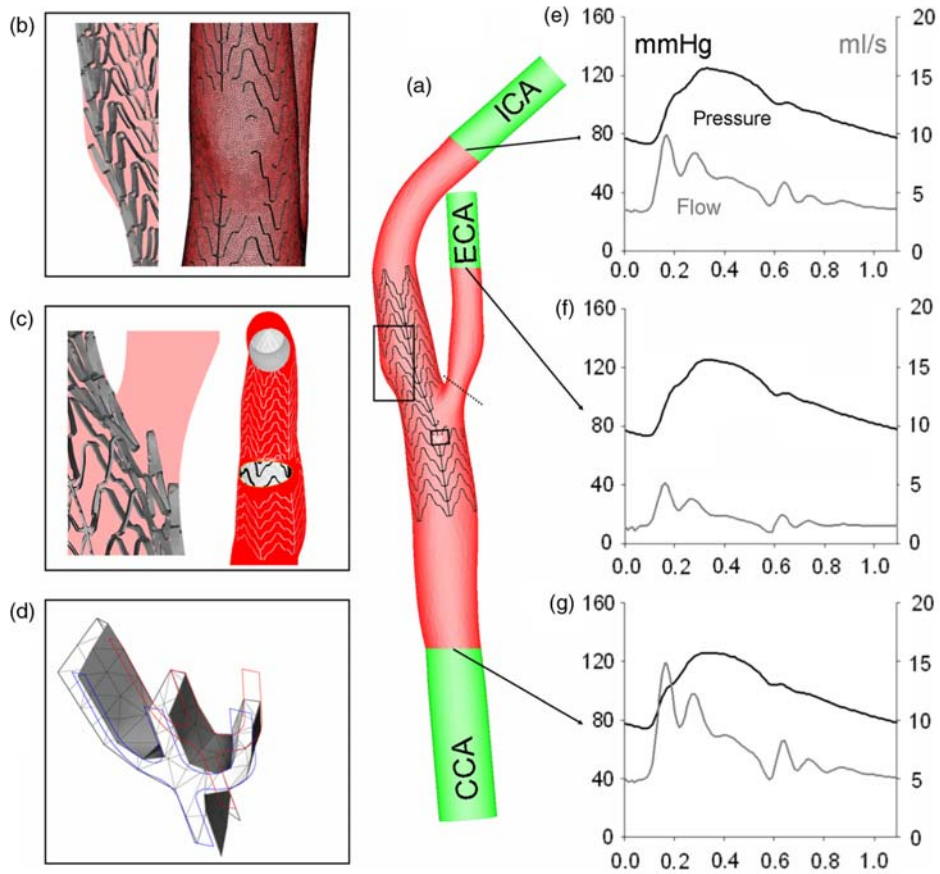

Figure 3. CFD mesh and flow at boundaries. (a) Arterial model reconstructed from FE simulation of CAS, with wet vessel surface (red), wet stent surface (grey) and flow extensions (green). The stent does not entirely conform to the vessel surface, leaving zones of malapposition (panel b, right), fish scaling (panels b and c, left) and unapposed struts partially occluding the ECA orifice (panel c, right). The stent struts are accurately reconstructed (panel d: the grey surface represents the CFD mesh of a strut interconnection while the coloured lines represent the contours of the Finite Element Analysis (FEA) mesh). Panel b shows part of the surface mesh. Pressure and flow data at CCA (e), ICA (f) and ECA (g); values on the x-axis in seconds.

is currently not an option in a stented vessel because of the high number of topologically equivalent blocks that would be needed for the volume decomposition (De Santis et al., in press).

2.3 CFD simulation of carotid perfusion

Flow data at the boundaries of the stented carotid could not be measured because the stent was not implanted in the patient. Therefore, instead of applying arbitrary flow or pressure waveforms, a set of BCs assumed to be insensitive to the 3D geometry of the lumen were imposed to model the proximal and distal vasculature, as suggested by Williams et al. (2010). As such, this set of BCs can be applied also to other geometries, including the non-stented carotid artery and the stented carotid artery with a different stent model. A total pressure was applied at the inlet of the model and the pressure at the outlets was set according to the following convolution integral, previously introduced by Olufsen (1999):

$$p(t) = \frac{1}{T}\int_0^T z(\tau)\cdot q(t-\tau)\cdot \mathrm{d}\tau, \qquad (1)$$

where T is the RR interval of a cardiac cycle, z is an impulse response characterising the distal vasculature and q is the flow exiting the fluid domain through the outlet surface at time instance t.

The impulse responses at the ICA and ECA outlets [as well as the total pressure imposed at the common carotid artery (CCA) inlet] were based on sampled pressure and flow waveforms obtained from the 1D model developed by Reymond et al. (2009). With $P_i(\omega)$ and $Q_i(\omega)$ being the Fourier transform of pressure and flow waveforms for each outlet i, the impedance spectrum $Z_i(\omega)$ was defined as

$$Z_i(\omega) = \frac{P_i(\omega)}{Q_i(\omega)}, \quad i = \mathrm{ICA},\ \mathrm{ECA}. \qquad (2)$$

The vascular impulse response $z(t)$ was then calculated by inverse Fourier transforming $Z(\omega)$, yielding an impulse response which decays to zero for t going to infinity. However, keeping in mind the periodic nature of the problem, this infinite impulse response could be condensed within one period by subsequently adding all periodic frames ($t \in [kT, (k+1)T]$; $k = 1,2,3\ldots$) to the first T seconds of the impulse response, eventually yielding $z(t)$, the impulse response as it was used here.

The time-dependent simulation was carried out using a finite volume solver (Ansys Fluent, 12.0, Canonsburg, PA, USA) for the continuity and the Navier–Stokes equations in laminar conditions, using second-order accuracy in space and time and double numerical precision. A no-slip condition was applied to the boundary wall and blood was treated as the Newtonian fluid [density, 1050 kg/m^3 and viscosity, 0.0035 Pa s (Morbiducci et al. 2011)]. Because it was not possible to apply the impedance as an outlet BC (the impedance is independent of the upstream 3D geometry), we have computed the static pressure (the pressure is dependent on both the downstream impedance and the upstream 3D geometry). To implement the impedance numerically, Equation (1) was discretised in time, so we write the pressure, p, at time step k as

$$p_k = \frac{1}{T}\sum_{j=0}^{N-1} z_j q_{k-j} \Delta t, \tag{3}$$

where N represents the number of time steps within a period and Δt a fixed time step. Ideally, one would solve the flow field together with the BCs discussed above in an implicit manner. However, since Fluent was used as a black-box solver, the BC equations could not be added implicitly and the Jacobian ($\mathbf{J}$) that links pressure changes (Δp) at the boundaries to flow changes (Δq) at the outlets had to be estimated at the beginning of each time step. For the case of two outlets (indices 1 and 2) and one inlet (index 3), the Jacobian equation writes

$$\begin{bmatrix} \Delta q_1 \\ \Delta q_2 \end{bmatrix} = \begin{bmatrix} \frac{\partial q_1}{\partial p_1} & \frac{\partial q_1}{\partial p_2} & \frac{\partial q_1}{\partial p_3} \\ \frac{\partial q_2}{\partial p_1} & \frac{\partial q_2}{\partial p_2} & \frac{\partial q_2}{\partial p_3} \end{bmatrix} \cdot \begin{bmatrix} \Delta p_1 \\ \Delta p_2 \\ \Delta p_3 \end{bmatrix} = \mathbf{J} \cdot \begin{bmatrix} \Delta p_1 \\ \Delta p_2 \\ \Delta p_3 \end{bmatrix}. \tag{4}$$

After perturbing the outlet pressures and calculating the resulting flow changes, the Jacobian was estimated through finite differences, following the approach described by Lanoye (2007). Summing the elements on each row of $\mathbf{J}$ should give zero, since q does not change when the boundary pressures are perturbed uniformly. As a result, the inlet pressure did not need to be perturbed to estimate $\mathbf{J}$. The Jacobian equation (Equation (4)) and the BC equation (Equation (3)) form a closed system of linear equations that was solved for every time step. This iterative procedure required one cycle for the initialisation of the convolution (Equation (3)). Four cycles of 1.09 s were simulated to ensure periodicity of the results, using an implicit time integration scheme with a fixed time increment of 10 ms. The number of iterations in each time step was limited by the solver in order to reduce the residuals of the velocity and continuity equations below 10^{-7} and 10^{-6}, respectively. On eight Central Processing Units (CPUs) of type 3.40 GHz, the computation required 1 week time.

A mesh sensitivity analysis was carried out under steady-state conditions to reduce the computational time. As the inlet flow that would establish after imposing total pressure and impedances was not known *a priori*, a worst-case scenario has been set by imposing an inlet flow of 23.6 ml/s ($Re \sim 1300$) (Holdsworth et al. 1999) and stress-free outlets. From seven meshes, ranging from 0.25 to 4.1 million tetrahedrons, a mesh of 2.7 million tetrahedrons was chosen based on CCA static pressure, ICA flow, area average wall shear stress (WSS) and maximum nodal WSS (Appendix Figure 1). We verified *a posteriori* that the peak flow computed using the impedance model (14.9 ml/s) was significantly smaller than the steady-state flow used for the mesh sensitivity analysis, assuring the adequacy of the chosen mesh resolution. Flow and pressure at the boundaries and WSS vectors on the wet wall surface were recorded from the last cycle for post-processing.

2.4 Post-processing of arterial wall and stent-related haemodynamic parameters

For the analysis of the WSS, the wall needed to be separated into a wet stent surface and a wet vessel surface. The contact between vessel and stent and the amount of interconnected struts make this a challenging operation. A visual application dedicated to surface separation was implemented in pyFormex to perform the separation progressively by using multiple feature angles. The iterative procedure included the following three steps:

(1) With a chosen feature angle, the surface is split into sub-surfaces which can be classified as endothelium, stent or mixed (a combination of endothelium and stent).
(2) If no sub-surface is in the mixed group, the separation is terminated. Otherwise, step (1) needs to be repeated on the residual mixed surfaces with a smaller feature angle.
(3) When no sub-surface is in the mixed group, the sub-surfaces of the endothelium and stent can be merged, obtaining the wet endothelium and wet stent surfaces.

After associating all the surface triangles to endothelium and stent, three time-averaged descriptors of the WSS vectors, the time-averaged WSS (TAWSS), the oscillating shear index (OSI) and the relative residence time (RRT), were computed on these separated domains

according to the following equations:

$$\mathrm{TAWSS} = \tfrac{1}{T}\int_0^T |\mathbf{WSS}(\mathbf{s},t)| \cdot \mathrm{d}t,$$

$$\mathrm{OSI} = 0.5\left[1 - \left(\frac{\left|\int_0^T \mathbf{WSS}(\mathbf{s},t)\cdot \mathrm{d}t\right|}{\int_0^T |\mathbf{WSS}(\mathbf{s},t)|\cdot \mathrm{d}t}\right)\right],$$

$$\mathrm{RRT} = \frac{1}{(1 - 2\cdot \mathrm{OSI})\cdot \mathrm{TAWSS}},$$

where T is the overall interval of the cardiac cycle and **s** is the position of a node on the vessel wall or the stent surface, t is the time of the last cardiac cycle and **WSS** is the wall shear stress vector. Low TAWSS values (lower than 0.4 Pa) (Malek et al. 1999), high OSI (He and Ku 1996) and high RRT (Lee et al. 2009) are known to promote an atherogenic endothelial phenotype, while abnormally high TAWSS values can be thrombogenic (Malek et al. 1999).

3. Results

The computational mesh of the lumen of the stented carotid artery contained 2,755,204 tetrahedrons, with an edge length of 0.19 mm on average (maximum 0.40 mm), a cell volume of 0.000784 mm^3 on average (maximum 0.002116 mm^3) and an equiangle skewness of 0.30 on average (maximum 0.87). To classify all triangles of the surface obtained from the Boolean subtraction, the novel procedure based on the multiple feature angles required 15 min of operator intervention and seven iterations. The iterations are described in detail in Table 1 and illustrated in Appendix Figure 2 and Appendix Figure 3.

When converting the final FE model of the carotid artery and deployed stent, all geometrical features of the vessel and stent appearing in the deformed configuration (e.g. strut size and cross-sectional shape) are preserved in the CFD model, except when the stent-to-vessel distance is lower than 20% of the stent strut thickness. In that case, contact between stent and vessel is assumed. Of the total stent surface (538.7 mm2), 15.5% (83.5 mm^2) is located on the outer side and can potentially scaffold the vessel wall but only 8.2% (44.13 mm^2) effectively contacts the vessel wall. This is due to (i) a region of malapposition (imperfect contact between stent and vessel) occurring distally to the stenosis, due to a limited capability of the stent to conform to the artery wall (contourability) and (ii) stent struts obstructing the ECA ostium. In these regions, fish-scaling effect appears with stent struts oriented transversally to the local vessel surface (Figure 3(b), (c)).

During the simulated cardiac cycle, the flow in the CCA is not equally partitioned in the daughter vessels, but a time-dependent flow split ratio governs the perfusion of ICA and ECA with the ICA taking from 63.5% to 79.4% of the flow (70.1% on average) (Figure 4). The haemodynamic characterisation of the wet vessel surface in terms of WSS metrics shows the presence of a large atherosusceptible region (TAWSS < 0.4 Pa) where malapposition occurred [outer edge of the ICA, distally to the stenosis; Figure 5(c)]. Moreover, all inter-strut connections (trifurcations) present the same atherosusceptible pattern on the proximal side (Figure 5(a), (b)). The distribution of the high RRT repeats the same trend of the low TAWSS, but the pattern around the strut interconnections attenuates distally (Figure 5(e)). This attenuation depends on OSI, which decreases in the proximal direction. However, the OSI does not indicate atherosusceptible regions *per se*, as it is lower than 0.15 throughout the surface (Figure 5(f)).

Two regions can be distinguished on the wet stent surface: in the bifurcation, the stent struts facing the ECA orifice are subjected to high TAWSS values, with instantaneous WSS vectors reaching a maximal intensity of 65 Pa during the cardiac cycle, while far from the bifurcation the stent struts experience a TAWSS that is one order of magnitude lower (Figure 5(d)). Post-stenting geometrical features (malapposition gaps, fish scaling

Table 1. Surface separation using a multiple feature angles.

Iteration	Feature angle	Endothelium area (mm^2)	Endothelium sub-surfaces	Stent area (mm^2)	Stent sub-surfaces	Mixed surface area (mm^2)	Mixed sub-surfaces
0	None	0	0	0	0	1844.42	1
1	85	0	0	5.16	12	1839.27	12
2	83	0	0	2.49	6	1836.78	29
3	80	10.4	3	5.18	12	1821.2	35
4	77	285.72	7	51.67	15	1483.81	27
5	75	38.86	4	141.01	11	1303.91	24
6	72	147.41	15	156.61	24	999.88	9
7	35	865.52	9	134.36	35	0	0
Total		1347.91	38	496.51	115	0	0

Note: The original surface is entirely subdivided into endothelium and stent in seven steps. In total, the user needs to decide upon only 153 sub-surfaces during the procedure, requiring 15 min of intervention. The sum of the total endothelium area (1347.91 mm^2) and the total stent area (496.51 mm^2) is equal to the area of the initial mixed surface (1844.42 mm^2).

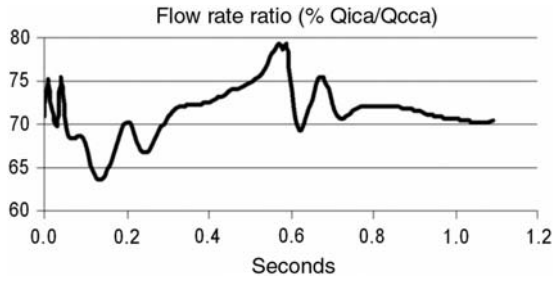

Figure 4. Flow rate ratio. It shows that during one cardiac cycle 70.1% of the flow passes through the ICA.

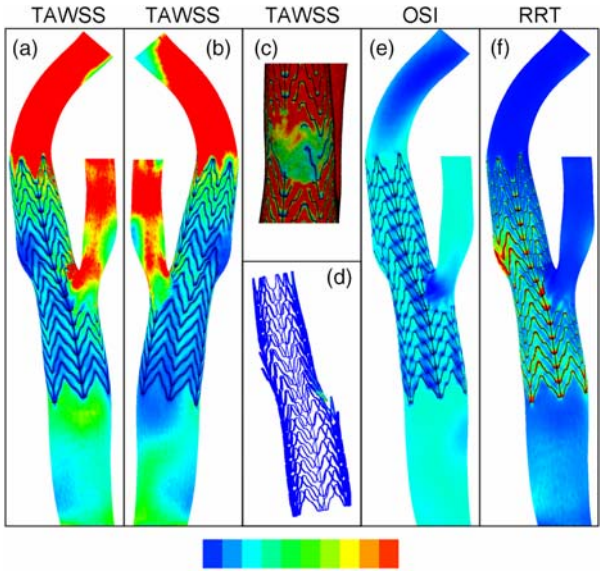

Figure 5. Time-average descriptors of the WSS on the vessel and the stent. In (a, b, c, e and f) the WSS indices are shown on the vessel while the stent is coloured in black. (a, b) TAWSS, front and back view (blue, 0.02 Pa; red, >3 Pa), (c) TAWSS, top view, showing the malapposed region (blue, 0.02 Pa; red, >0.4 Pa), (d) TAWSS on the wet stent surface (blue, <7 Pa; red, 27.7 Pa), (e) OSI, front view (blue, 0; red, 0.5) and (f) RRT, front view (blue, 0.05 Pa^{-1}; red, >10 Pa^{-1}).

and struts facing the orifice) predicted from FEA colocalise with altered haemodynamics features predicted from CFD.

4. Discussion

4.1 Vessel geometry and strut malapposition impact the near-wall haemodynamics

In this study, the haemodynamic impact of CAS is explored using both a stent- and a patient-specific analysis. A stent is deployed in a carotid artery using the FEM, and both deformed vessel and stent are taken into account for the flow computation. Low TAWSS values on the vessel surface colocalise with the distal side of stent strut interconnections and regions of malapposition. Strut interconnections represent an obstacle to flow due to the strut thickness. Malapposition does not induce low TAWSS *per se* but occurs where the pre-stenting vessel shows a concave profile. Even after CAS, the stent is not able to accomplish the concave surface neither to straighten it up. Thus, in both cases, low TAWSS appears where the surface is shielded from the main stream. Such correspondence of location of imperfect scaffolding and atheroprone haemodynamics suggests that the geometrical characterisation of the stented configuration may be used as a surrogate for the (more time-consuming) CFD analysis, thus significantly simplifying the assessment of haemodynamics impact of a stent on a vessel. On the stent side, struts appear in the ECA ostium and represent an obstacle to the stream. On such struts, elevated shear forces may represent a risk for embolism. Recent OCT imaging observations have suggested that struts facing the orifice may endothelialise (Tanigawa et al. 2007). If living cells colonialise the struts facing the ECA orifice, the abnormally high WSS may trigger thromboembolic events (Malek et al. 1999). In such a case, the detached embolus could be either flown into the ECA or sucked into the ICA stream, depending on the flow features at that location and at that phase of the cardiac cycle, thereby possibly causing a stroke.

4.2 Technological improvements

From a technical perspective, the major innovations presented in this work include (i) a tool to convert an FEA mesh into a CFD mesh of a patient-specific stented artery using a triggering operation and (ii) a tool to divide a wet stent from wet vessel by visual examination for separated post-processing. The conversion of an FEA mesh into a CFD mesh requires performing a subtraction of volumes. Because of the realistic image-based and FE-based geometries and because of the (imperfect) contact between the stent and the vessel, the subtraction produces a surface which cannot be directly used to generate a volume mesh. The triggering operation presented in this study allows generating a meshable volume with a Boolean subtraction. After generating the volume mesh, the surface representing the wet boundary needs to be divided into a wet endothelium surface and a wet stent surface. Thanks to the novel multiple feature angle procedure, the separation of the surface can be successfully carried out graphically in a matter of minutes. A single-step approach, which is the usual procedure to separate surfaces (e.g. to select the boundary sections for the imposition of the BCs), would be impractical because (1) partitioning the original surface with an angle of 35° would produce about 1000 surfaces requiring several hours or days of user intervention, (2) it would be hard to visualise the surfaces and to decide whether they belong to the endothelium or

the stent and (3) it would not be possible to know *a priori* whether the chosen feature angle was sufficiently small to separate all surfaces, with the risk of having to repeat the procedure from the beginning with a new smaller feature angle.

With such improvements, a number of simplifications assumed in previous works no longer seem to be required. Virtual stenting (geometrical stent expansion in a rigid vessel) has been proposed to replace the FE analysis (Appanaboyina et al. 2008). However, it may introduce an error in the haemodynamic parameters because it approximates the post-stenting vessel using the unstented vessel and it considers the stent as a geometrical entity only. Two stents with the same design but different stiffness would result in the same vessel–stent configuration after virtual stenting and, in turn, in the same haemodynamic effect. This approach does not allow to consider and quantify (also clinically) important stent-related aspects such as lumen gain, vessel straightening, stent malapposition, fish-scaling effect and asymmetric stent strut deployment which occur in reality and can be captured using an FE analysis before solving the flow (Conti et al. 2011).

The geometrical complexity of a patient-specific analysis has motivated the use of simplified vessel geometries, such as an idealised vessel model (straight or curved cylinder), non-bifurcating vessels, non-stenosed (healthy vessels) or simplified stent designs, such as reduced stent size (to limit the computational domain, which requires very fine mesh around the stent struts) and non-realistic cross sections of the struts (LaDisa et al. 2003; Balossino et al. 2008; Kim et al. 2008; Radaelli et al. 2008; Larrabide et al. 2010; Pant et al. 2010). For the first time, flow in a patient-specific stented bifurcating vessel has been imposed using an impedance model, following the recent contributions of Williams et al. (2010) (idealised stented coronary artery bifurcation) and Morbiducci, Gallo, Massai et al. (2010) (patient-specific unstented carotid artery). Prescribing a generic flow waveform as inlet BC and/or a fixed flow ratio as outlet BCs would not suit the goal of this study since the hydraulic resistance of a stented carotid bifurcation may be different from the unstented case, and this effect would be lost when flow waveforms obtained from an unstented geometry would be imposed (Williams et al. 2010). Therefore, a total pressure was prescribed at the CCA inlet, and the vasculature distal to each outlet was modelled as a time-invariant linear dynamic system, completely determined by its impedance spectrum, represented as a vascular impulse response. The pressure and flow waveforms that were used to generate the BCs were taken from the 1D model (Reymond et al. 2009), which has been validated against *in vivo* data and yields generic but realistic pressure waveforms throughout the vascular tree. It is, however, important to note that the obtained waveforms (upon which we based our BCs) characterise the proximal vasculature and distal vasculature. Therefore, by following this approach, we assume that (i) the total pressure at the CCA is insensitive to the presence of the stent downstream and (ii) the impedance of the downstream vasculature is insensitive to the presence of the stent upstream.

4.3 Limitations and final remarks

In a recent retrospective investigation, the aortic flow was evaluated before and after a graft implantation using patient-specific geometries and personalised BCs (Karmonik et al. 2011). Because this was not possible in our prospective analysis, we have chosen to use a set of BCs which could be applied before and after a stent implantation, and also with different stent models, renouncing to the application of personalised flow waveforms (Morbiducci, Gallo, Massai et al. 2010; Morbiducci, Gallo, Ponzini et al. 2010). It is currently difficult to get patient-specific impedance values because it requires measuring both the pressure and flow waveforms during the same cardiac cycle *in vivo*. In future, further research and clinical data may provide indications on how to convert subject-specific flow conditions, measured before stenting, to the carotid flow conditions after stenting. Additionally, the measured blood haematocrit can be included into a more sophisticated rheological model to improve the representation of the near-wall haemodynamics, with higher accuracy of the predicted TAWSS and the RRT (Lee and Steinman 2007; Morbiducci et al. 2011).

The present methodology represents a valid solution to perform a CFD calculation based on the post-stenting configuration, in turn based on an FE replica of CAS starting from images of the unstented vessel and stent, and can be expanded to other vessel–stent interventions such as balloon-expandable stents for coronary stenting (Mortier et al. 2010), implantation of self-expanding flow diverters in cerebral aneurysms (Radaelli et al. 2008) and implantation of stented graft in abdominal aortic aneurysms (Li and Kleinstreuer 2005; Kleinstreuer et al. 2007; Kleinstreuer et al. 2008). This full-scale approach accurately reproduces the geometry and flow after stenting and could be used for clinical training or, after *a posteriori* validation, for CAS planning. However, it is not suitable for a large population analysis, but limited to single cases because (1) both FEA and CFD computations require significant CPU time and memory and (2) the model conversion from FEA to CFD needs operator skills and time which make the use of such a methodology currently improbable for clinical applications. Within this context, simplified models aiming at a faster computation of the haemodynamics in stented arteries should be appreciated (Larrabide et al. 2010).

Acknowledgements

Gianluca De Santis' research is supported by a BOF grant from Ghent University. Joris Degroote gratefully acknowledges a postdoctoral fellowship of the Research Foundation Flanders (FWO).

References

Appanaboyina S, Mut F, Lohner R, Putman CA, Cebral JR. 2008. Computational fluid dynamics of stented intracranial aneurysms using adaptive embedded unstructured grids. Int J Numer Methods Fluids. 57(5):475–493.

Auricchio F, Taylor RL, Lubliner J. 1997. Shape-memory alloys: macromodelling and numerical simulations of the superelastic behavior. Comput Methods Appl Mech Eng. 146(3–4): 281–312.

Auricchio F, Conti M, De Beule M, De Santis G, Verhegghe B. 2011. Carotid artery stenting simulation: from patient-specific images to finite element analysis. Med Eng Phys. 33(3):281–289.

Balossino R, Gervaso F, Migliavacca F, Dubini G. 2008. Effects of different stent designs on local hemodynamics in stented arteries. J Biomech. 41(5):1053–1061.

Bangalore S, Kumar S, Wetterslev J, Bavry AA, Gluud C, Cutlip DE, Bhatt DL. 2011. Carotid artery stenting vs carotid endarterectomy meta-analysis and diversity-adjusted trial sequential analysis of randomized trials. Arch Neurol. 68(2):172–184.

Brott TG, Hobson RW, Howard G, Roubin GS, Clark WM, Brooks W, Mackey A, Hill MD, Leimgruber PP, Sheffet AJ. 2010. Stenting versus endarterectomy for treatment of carotid-artery stenosis. New Engl J Med. 363(1):11–23.

Carnelli D, Pennati G, Villa T, Baglioni L, Reimers B, Migliavacca F. 2011. Mechanical properties of open-cell, self-expandable shape memory alloy carotid stents. Artif Organs. 35(1):74–80.

Conti M, van Loo D, Auricchio F, De Beule M, De Santis G, Verhegghe B, Pirrelli S, Odero A. 2011. Impact of carotid stent cell design on vessel scaffolding: a case study comparing experimental investigation and numerical simulations. J Endovasc Ther. 18(3):397–406.

Cosottini M, Michelassi MC, Bencivelli W, Lazzarotti G, Picchietti S, Orlandi G, Parenti G, Puglioli M. 2010. In stent restenosis predictors after carotid artery stenting. Stroke Res Treat. March 14. doi:10.4061/2010/864724.

De Santis G, Mortier P, De Beule M, Segers P, Verdonck P, Verhegghe B. 2010. Patient-specific computational fluid dynamics: structured mesh generation from coronary angiography. Med Biol Eng Comput. 48(4):371–380.

De Santis G, De Beule M, Segers P, Verdonck P, Verhegghe B. 2011. Patient-specific computational haemodynamics: generation of structured and conformal hexahedral meshes from triangulated surfaces of vascular bifurcations. Comput Methods Biomech Biomed Eng. 14(9): 797–802.

De Santis G, De Beule M, van Canneyt K, Segers P, Verdonck P, Verhegghe B. in press. Full-hexahedral structured meshing for image-based computational vascular modeling. Med Eng Phys.

Ederle J, Dobson J, Featherstone RL, Bonati LH, van der Worp HB, de Borst GJ, Lo TH, Gaines P, Dorman PJ, Macdonald S, Lyrer PA. 2010. Carotid artery stenting compared with endarterectomy in patients with symptomatic carotid stenosis (international carotid stenting study): an interim analysis of a randomised controlled trial. Lancet. 375(9719): 985–997.

Ener RA, Fiss D, Georgakis A, Wolf NM, Pandit N, Piegari GN. 2008. Carotid artery in-stent restenosis after carotid artery stenting. J Invasive Cardiol. 20(6):286–291.

Groschel K, Riecker A, Schulz JB, Ernemann U, Kastrup A. 2005. Systematic review of early recurrent stenosis after carotid angioplasty and stenting. Stroke. 36(2):367–373.

He XJ, Ku DN. 1996. Pulsatile flow in the human left coronary artery bifurcation: average conditions. J Biomech Eng Trans ASME. 118(1):74–82.

Holdsworth DW, Norley CJD, Frayne R, Steinman DA, Rutt BK. 1999. Characterization of common carotid artery blood-flow waveforms in normal human subjects. Physiol Measure. 20(3):219–240.

Karmonik C, Bismuth J, Davies MG, Shah DJ, Younes HK, Lumsden AB. 2011. A computational fluid dynamics study pre- and post-stent graft placement in an acute type B aortic dissection. Vasc Endovasc Surg. 45(2):157–164.

Kim M, Taulbee DB, Tremmel M, Meng H. 2008. Comparison of two stents in modifying cerebral aneurysm hemodynamics. Ann Biomed Eng. 36(5):726–741.

Kleinstreuer C, Li Z, Farber MA. 2007. Fluid–structure interaction analyses of stented abdominal aortic aneurysms. Annu Rev Biomed Eng. 9:169–204.

Kleinstreuer C, Li Z, Basciano CA, Seelecke S, Farber MA. 2008. Computational mechanics of Nitinol stent grafts. J Biomech. 41(11):2370–2378.

LaDisa JF, Guler I, Olson LE, Hettrick DA, Kersten JR, Warltier DC, Pagel PS. 2003. Three-dimensional computational fluid dynamics modeling of alterations in coronary wall shear stress produced by stent implantation. Ann Biomed Eng. 31(8):972–980.

Lanoye L. 2007. Fluid–structure interaction of blood vessels. [PhD thesis], Ghent University, Gent, Belgium.

Larrabide I, Kim M, Augsburger L, Villa-Uriol MC, Rüfenacht D, Frangi AF. 2010. Fast virtual deployment of self-expandable stents: method and *in vitro* evaluation for intracranial aneurysmal stenting. Med Image Anal.

Lee S-W, Steinman DA. 2007. On the relative importance of rheology for image-based CFD models of the carotid bifurcation. J Biomech Eng Trans ASME. 129(2):273–278.

Lee S-W, Antiga L, Steinman DA. 2009. Correlations among indicators of disturbed flow at the normal carotid bifurcation. J Biomech Eng Trans ASME. 131(6): 061013.

Li ZH, Kleinstreuer C. 2005. Blood flow and structure interactions in a stented abdominal aortic aneurysm model. Med Eng Phys. 27(5):369–382.

Malek AM, Alper SL, Izumo S. 1999. Hemodynamic shear stress and its role in atherosclerosis. J Am Med Assoc. 282(21):2035–2042.

Morbiducci U, Gallo D, Massai D, Consolo F, Ponzini R, Antiga L, Bignardi C, Deriu MA, Redaelli A. 2010. Outflow conditions for image-based hemodynamic models of the carotid bifurcation: implications for indicators of abnormal flow. J Biomech Eng Trans ASME. 132(9): 091005.

Morbiducci U, Gallo D, Ponzini R, Massai D, Antiga L, Montevecchi FM, Redaelli A. 2010. Quantitative analysis of bulk flow in image-based hemodynamic models of the carotid bifurcation: the influence of outflow conditions as test case. Ann Biomed Eng. 38(12):3688–3705.

Morbiducci U, Gallo D, Massai D, Ponzini R, Deriu M, Antiga L, Redaelli A, Montevecchi FM. 2011. On the importance of blood rheology for bulk flow in hemodynamic models of the carotid bifurcation. J Biomech. 44(13):2427–2438.

Mortier P, Holzapfel GA, De Beule M, Van Loo D, Taeymans Y, Segers P, Verdonck P, Verhegghe B. 2010. A novel

simulation strategy for stent insertion and deployment in curved coronary bifurcations: comparison of three drug-eluting stents. Ann Biomed Eng. 38(1):88–99.

Olufsen MS. 1999. Structured tree outflow condition for blood flow in larger systemic arteries. Am J Physiol Heart Circ Physiol. 276(1):H257–H268.

Pant S, Bressloff NW, Forrester AIJ, Curzen N. 2010. The influence of strut-connectors in stented vessels: a comparison of pulsatile flow through five coronary stents. Ann Biomed Eng. 38(5):1893–1907.

Paraskevas KI, Mikhailidis DP, Veith FJ. 2010. Mechanisms to explain the poor results of carotid artery stenting (CAS) in symptomatic patients to date and options to improve CAS outcomes. J Vasc Surg. 52(5):1367–1375.

Prendergast PJ, Lally C, Daly S, Reid AJ, Lee TC, Quinn D, Dolan F. 2003. Analysis of prolapse in cardiovascular stents: a constitutive equation for vascular tissue and finite-element modelling. Trans ASME. J Biomech Eng. 125(5):692–699.

Radaelli AG, Augsburger L, Cebral JR, Ohta M, Rüfenacht DA, Balossino R, Benndorf G, Hose DR, Marzo A, Metcalfe R, Mortier P, Mut F, Reymond P, Socci L, Verhegghe B, Frangi AF. 2008. Reproducibility of haemodynamical simulations in a subject-specific stented aneurysm model – a report on the virtual intracranial stenting challenge 2007. J Biomech. 41(10):2069–2081.

Reymond P, Merenda F, Perren F, Rufenacht D, Stergiopulos N. 2009. Validation of a one-dimensional model of the systemic arterial tree. Am J Physiol Heart Circ Physiol. 297(1):H208–H222.

Shah PK. 2003. Inflammation, neointimal hyperplasia, and restenosis – as the leukocytes roll, the arteries thicken. Circulation. 107(17):2175–2177.

Tanigawa J, Barlis P, Di Mario C. 2007. Do unapposed stent struts endothelialise? *In vivo* demonstration with optical coherence tomography. Heart. 93(3):378.

Williams AR, Koo BK, Gundert TJ, Fitzgerald PJ, LaDisa JF. 2010. Local hemodynamic changes caused by main branch stent implantation and subsequent virtual side branch balloon angioplasty in a representative coronary bifurcation. J Appl Physiol. 109(2):532–540.

Appendix

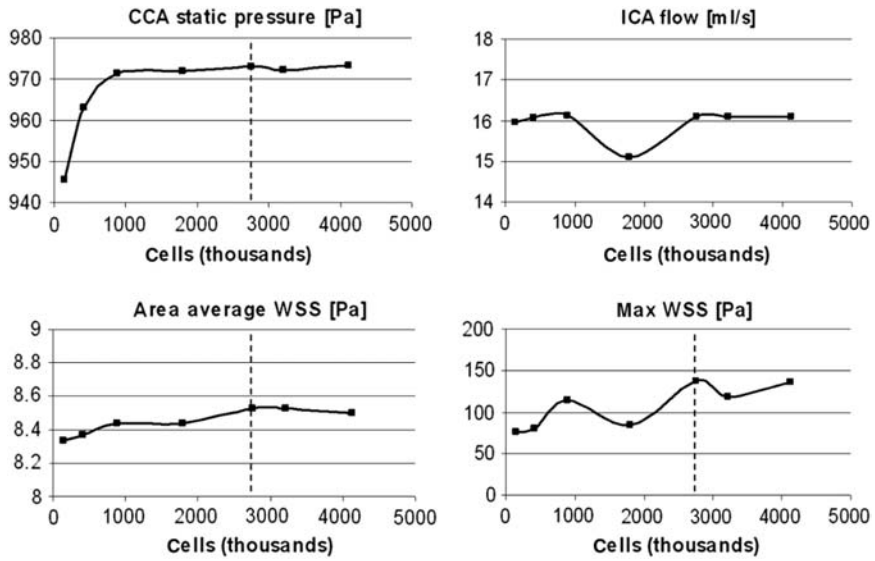

Appendix Figure 1. Mesh sensitivity analysis. From top-left to bottom-right: area average static pressure on the CCA cross section, flow exiting the ICA, area average WSS on stented-vessel surface and maximum nodal WSS. A steady-state flow inlet was imposed at the inlet and zero pressure at the outlets. All values plateau in the three finer meshes, with the exception of the maximum nodal WSS that oscillates. Such oscillations have been previously reported and depend on the numerical diffusion error associated with unstructured tetrahedral meshes rather than the mesh resolution (De Santis et al. 2010). The difference between the mesh of 2.7 million cells (indicated by a dotted line) and the mesh of 4.1 million cells (the finest mesh) was of 0.05%, 0.01%, 0.3% and 0.26% for the area average static pressure on the CCA cross section, flow exiting the ICA, area average WSS on stented-vessel surface and maximum nodal WSS, respectively.

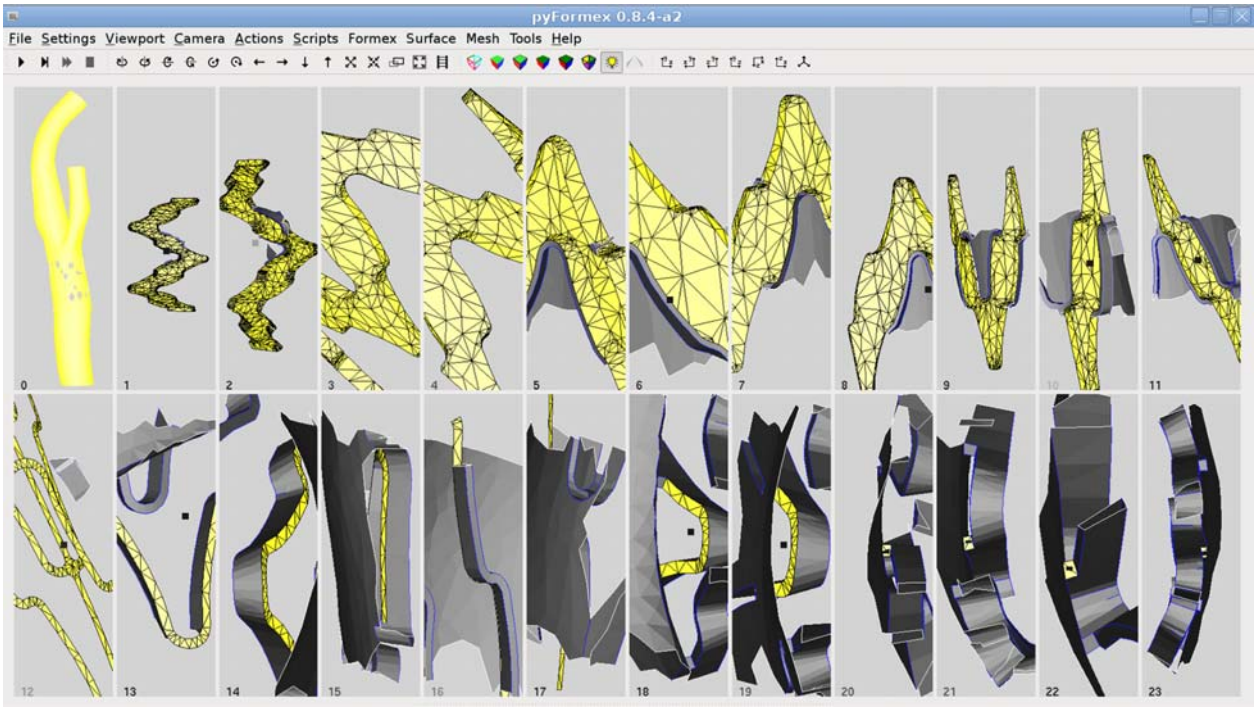

Appendix Figure 2. pyFormex interface dedicated to the surface separation using multiple feature angles. The user needs to attribute the yellow sub-surface of each panel to a group (the grey surface is drawn to help to recognise the sub-surface). In this frame, no panel contains the endothelium, 12 panels contain the stent (from 12 to 23) and 12 panels contain both endothelium and stent (mixed, from 0 to 11). The sub-surfaces in the corresponding groups are shown in Appendix Figure 3 (top).

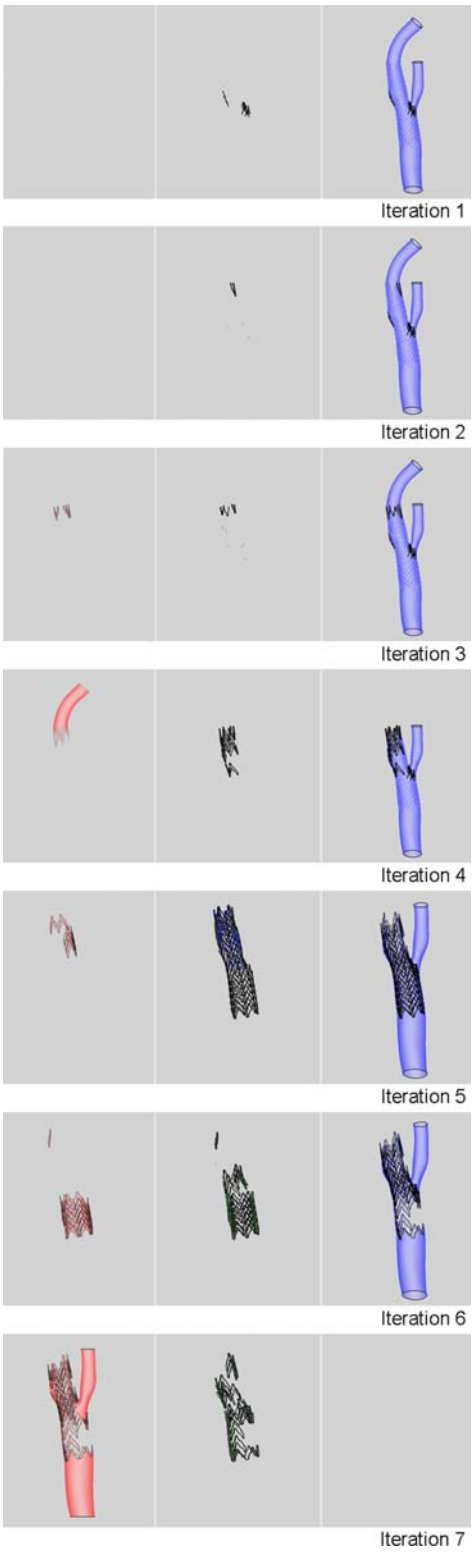

Appendix Figure 3. Endothelium, stent and mixed surfaces at each iteration. At the beginning, the surface is entirely in the mixed group. Then, using increasingly smaller feature angles (iterations 1–7 are reported in Table 1), the mixed surface is progressively reduced and assigned to the endothelium and stent surfaces. At the (i)-iteration, the left and middle panels represent the portion of the endothelium and stent separated from the mixed surface of the ($i - 1$)-iteration while the right panel represents the remaining mixed surface at the (i) iteration. At the last iteration, no triangles belong to the mixed surface.